Supplemental Information for Imaging correlated nuclear motion mediated by passage through a conical intersection

Tu Thanh Nguyen[1], Smita Ganguly[1], Sajed Hosseini Zavareh[1], Sanduni Kudagama[1,2], Avijit Duley[1], Anbu Selvam Venkatachalam[1], Eric Mullins[1], Cosmin Blaga[1], Huynh Van Sa Lam[1], Vinod Kumarappan[1], Artem Rudenko[1], Daniel Rolles[1*], Ruaridh Forbes[3*]

[1*]James R. Macdonald Laboratory, Physics Department, Kansas State University, Manhattan, 66506, KS, USA.
[2]European XFEL GmbH, Schenefeld, Germany.
[3]Department of Chemistry, University of California Davis, Davis, 95616, CA, USA.

*Corresponding author(s). E-mail(s): rolles@ksu.edu; ruforbes@ucdavis.edu;
Contributing authors: nttu14780@ksu.edu; smitag@ksu.edu; sajed1@ksu.edu; sanduni.kudagama@xfel.eu; avijitd@ksu.edu; anbu@ksu.edu; mullinsel@ksu.edu; blaga@ksu.edu; huynhlam@ksu.edu; kumarappan@ksu.edu; rudenko@ksu.edu;

References

[1] Bogumil, K., Orphal, J., Homann, T., Voigt, S., Spietz, P., Fleischmann, O.C., Vogel, A., Hartmann, M., Kromminga, H., Bovensmann, H., Frerick, J., Burrows, J.P.: Measurements of molecular absorption spectra with the sciamachy pre-flight model: instrument characterization and reference data for atmospheric remote-sensing in the 230–2380 nm region. Journal of Photochemistry and Photobiology A: Chemistry **157**(2), 167–184 (2003) https://doi.org/10.1016/S1010-6030(03)00062-5 . Atmospheric Photochemistry

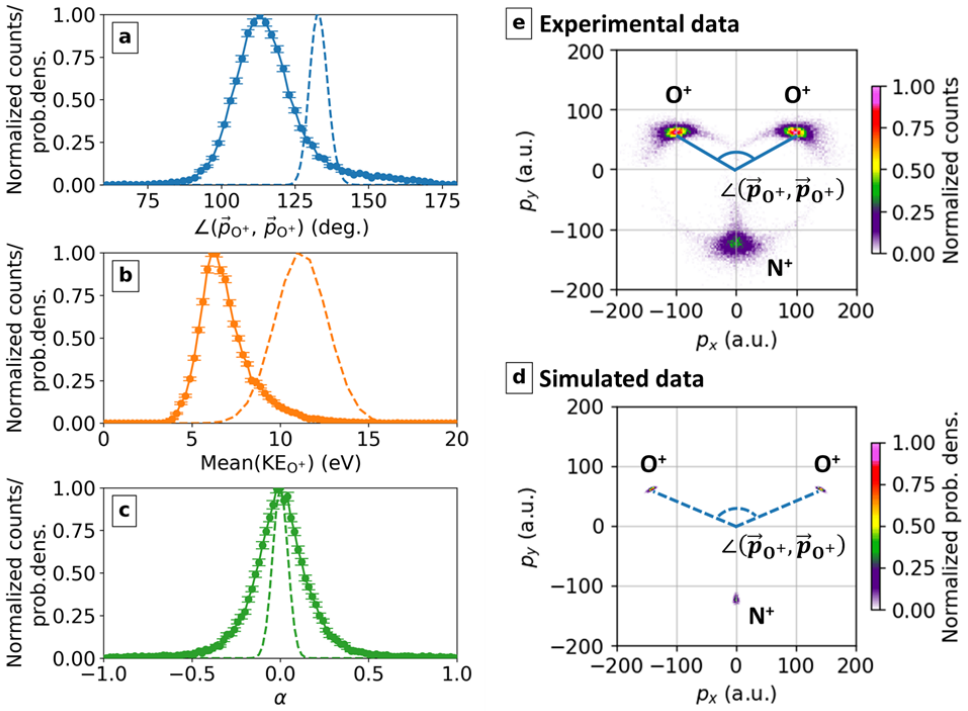

Fig. 1 Comparison between experimental Coulomb explosion data and classical Coulomb explosion simulations. Measured (probe-only) momentum-space distributions of the (N^+, O^+, O^+) coincidence channel (solid lines) compared with the initial ground-state nuclear probability density projected onto the momentum-space observables, generated by performing classical Coulomb explosion simulations (dashed lines) as described in the Methods section. Distributions are shown for **(a)** the angle between the two O^+ fragment momenta $\angle(\vec{p}_{O^+}, \vec{p}_{O^+})$ (blue), **(b)** the mean kinetic energy of two O^+ fragments (orange), and **(c)** the asymmetric parameter α (green). The vertical error bars represent the counting error (1σ) of the experimental data. While there is overall qualitative agreement between simulations and experiment that can be used to relate the measured fragment momenta to the underlying molecular geometry, there are some quantitative differences, which are the result of the non-Coulombic nature of the tri-cationic potential energy surface and which lead to an overestimation of the momentum-space angle and the mean kinetic energy of two O^+ fragments in the purely Coulombic simulations. **(d,e)** Newton plots for the (O^+, N^+, O^+) triple coincidence from the experimental data **(d)** and Coulomb explosion simulations **(e)** starting from molecular geometries near the ground-state equilibrium geometry. In these Newton plots, the p_x and p_y axes are defined by the difference and the sum of the two O^+ momenta, respectively. The blue solid lines in **(d)** indicate the measured $\angle(\vec{p}_{O^+}, \vec{p}_{O^+})$ angle, with blue dashed lines in **(e)** showing the corresponding angle in the simulated Coulomb explosion.

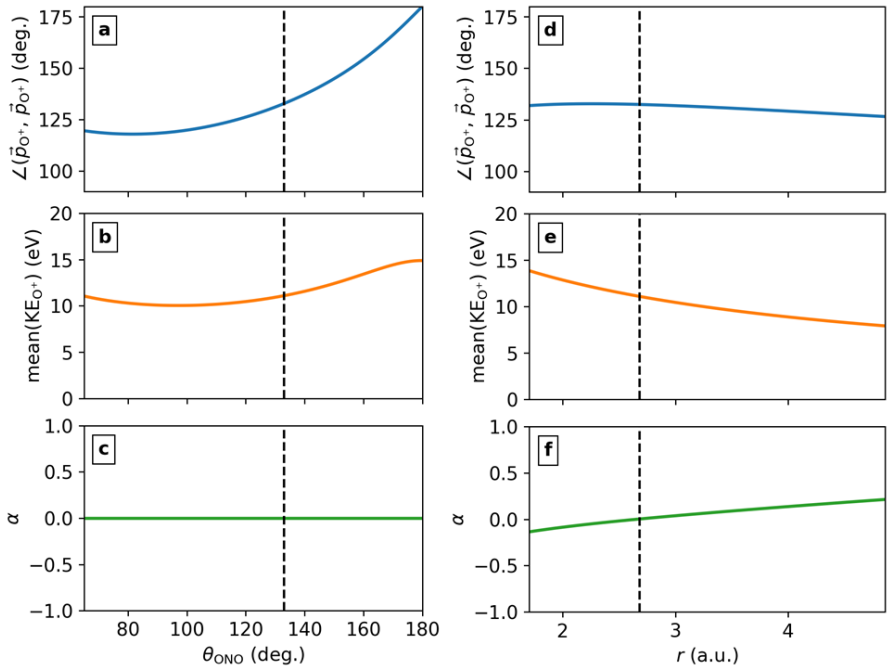

Fig. 2 Dependence of the momentum-space observables on the real-space molecular geometry according to the Coulomb explosion simulations. (a–c) Momentum-frame angle $\angle(\vec{p}O^+, \vec{p}O^+)$ **(a)**, mean kinetic energy of the two O^+ fragments **(b)**, and kinetic energy asymmetry parameter α **(c)** as functions of the real-space bond angle θ_{ONO}, with both N–O bond lengths fixed at 2.68 a.u. The black vertical lines at 133° mark the equilibrium bond angle of the ground-state geometry. **(d–f)** The same momentum-space observables shown in **(a–c)** plotted as functions of one N–O bond length r, with the other N–O bond fixed at 2.68 a.u. and the bond angle θ_{ONO} fixed at 133°. The black vertical lines at 2.68 a.u. indicate the equilibrium bond length in the ground-state configuration.

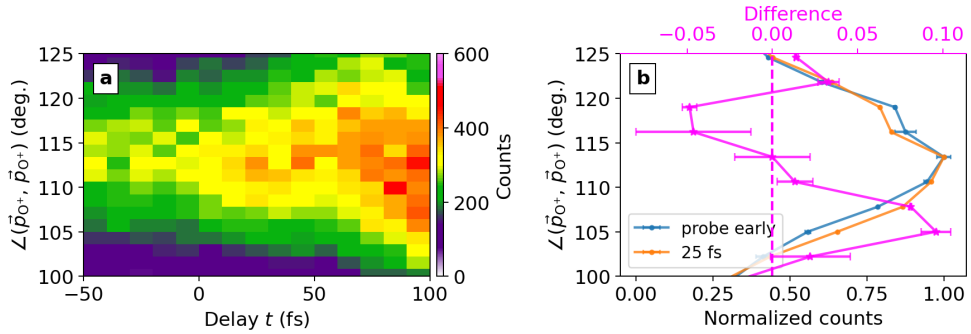

Fig. 3 Highlighting the decrease of the momentum-space angle at early pump-probe delays. (a) Zoom-in of **Fig. 2** of the main text. (b) Measured momentum-space angle $\angle(\vec{p}_{O^+}, \vec{p}_{O^+})$ when the probe pulse arrives early (blue), as compared to when it arrives 25 fs after the pump pulse (orange). The magenta line (top axis) is the difference between the yield at the two delays.

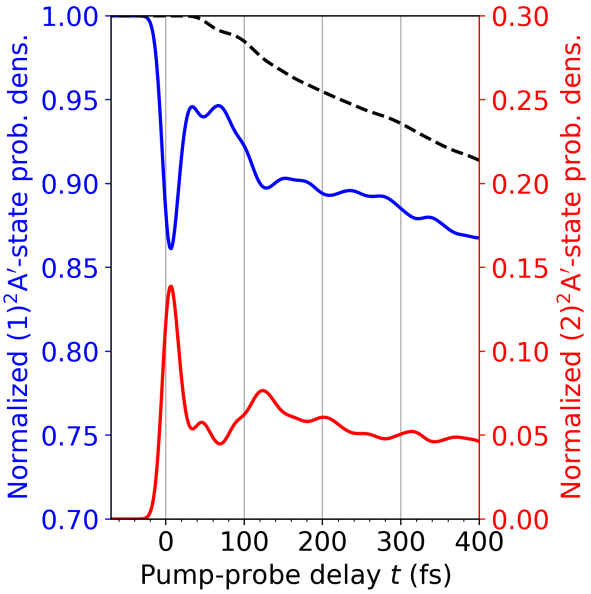

Fig. 4 Time-dependent normalized adiabatic nuclear wavepacket probability densities in the $(1)^2\mathrm{A}'$ **and** $(2)^2\mathrm{A}'$ **states.** The $(1)^2\mathrm{A}'$-state population is denoted in blue with the scale on the left, and the $(2)^2\mathrm{A}'$-state population is denoted in red with the scale on the right. The time-dependent normalized total population is depicted as black dashed line (left scale).

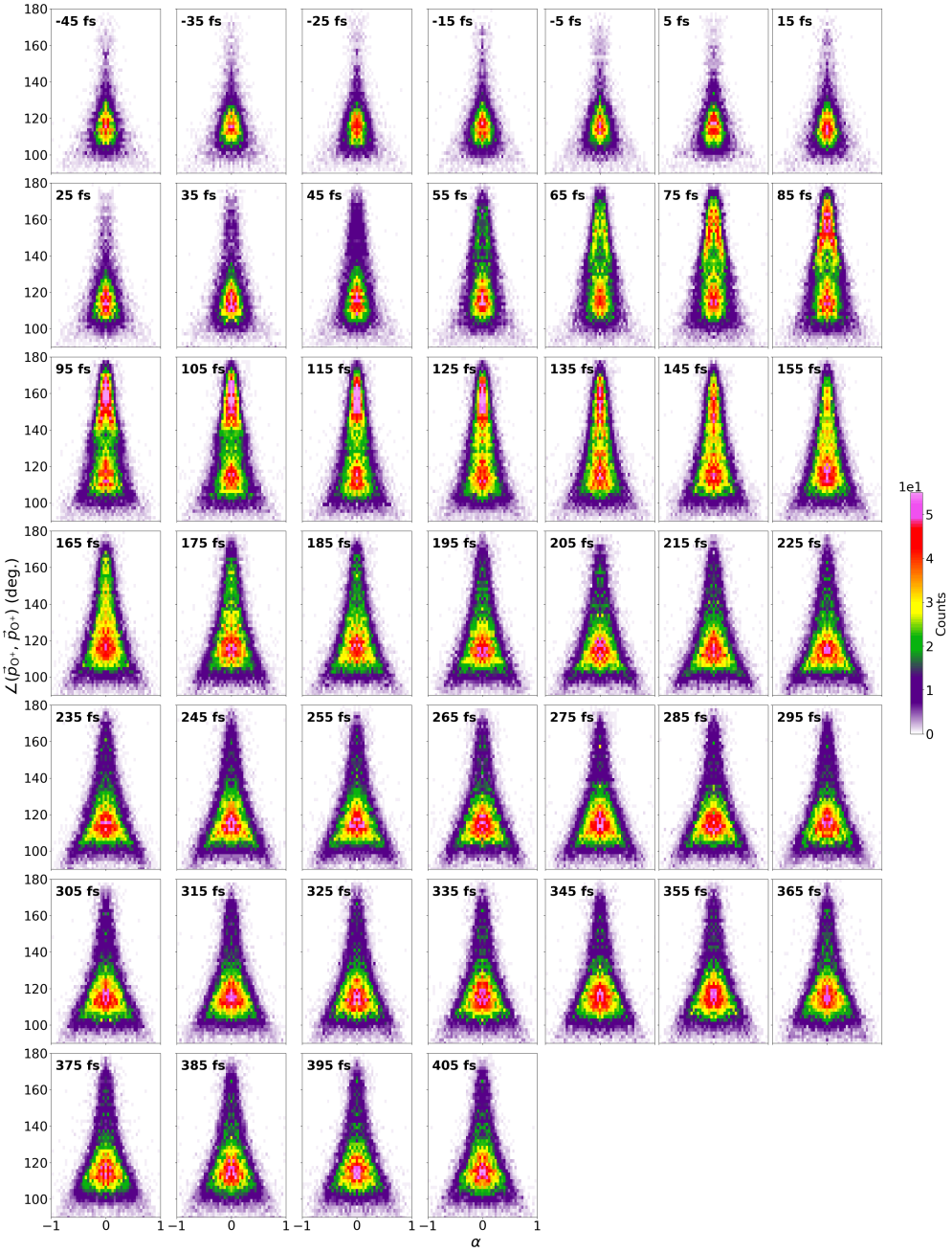

Fig. 5 Experimental unsubtracted momentum-space correlation maps between the momentum-frame angle $\angle(\vec{p}_{\mathrm{O}^+}, \vec{p}_{\mathrm{O}^+})$ and asymmetric parameter α as a function of delay from -45 to 405 fs, binned in time steps of 10 fs.

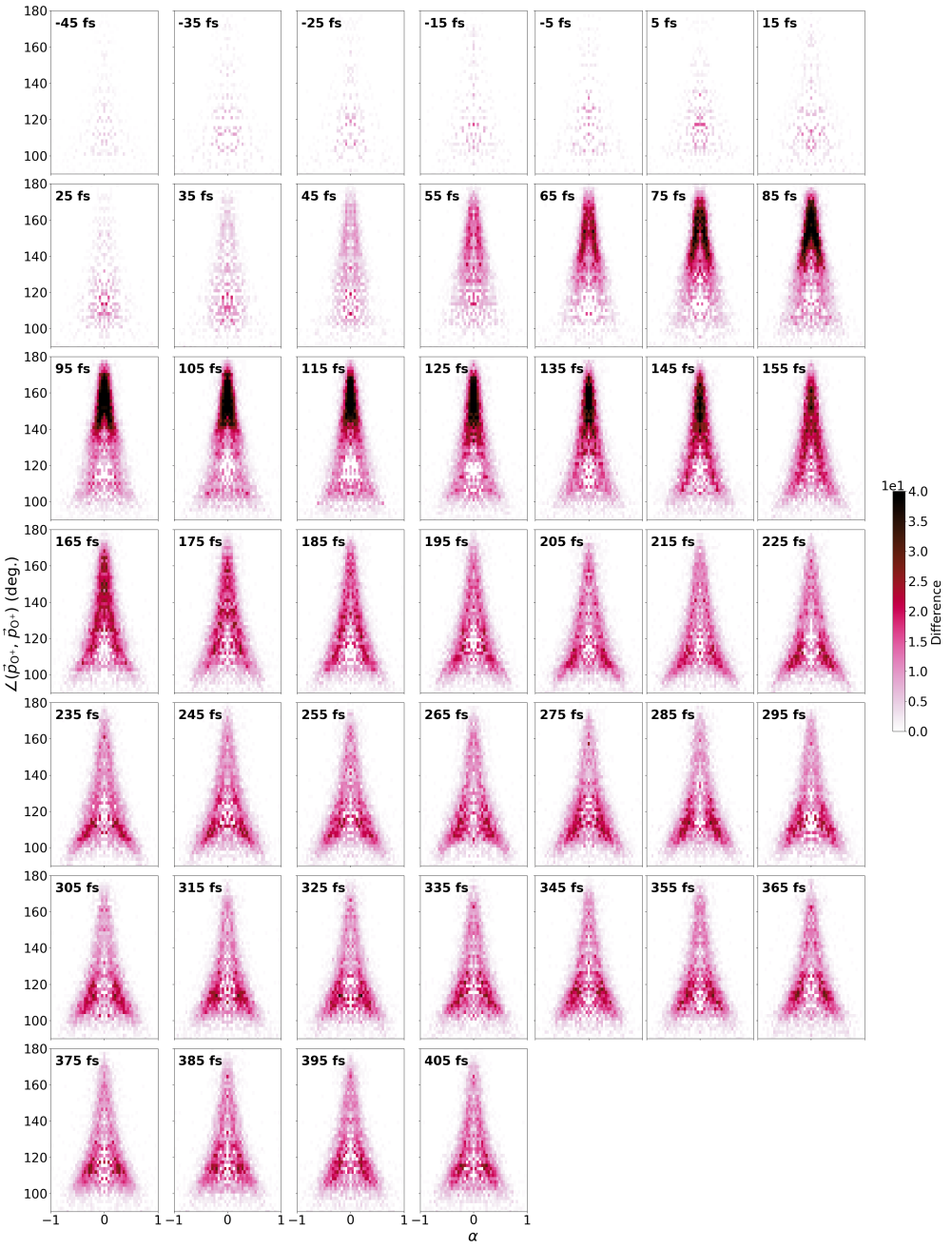

Fig. 6 Experimental subtracted momentum-space correlation maps between the momentum-frame angle $\angle(\vec{p}_{O+}, \vec{p}_{O+})$ and asymmetric parameter α as a function of delay from -45 to 405 fs, binned in time steps of 10 fs. All panels show delay-dependent maps after subtraction of the mean signal recorded at negative pump-probe delay ($t < -50$ fs) to highlight pump-induced changes.

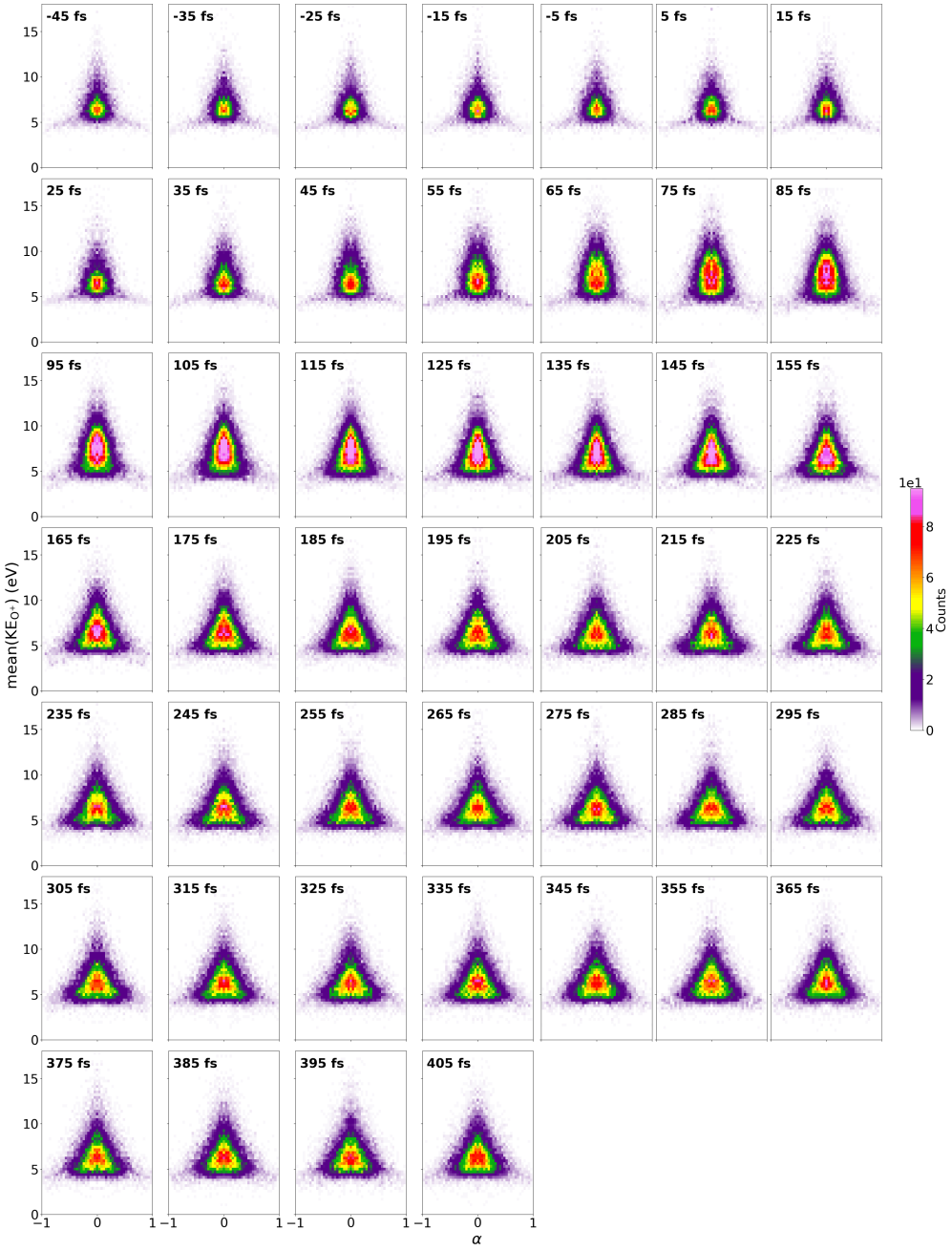

Fig. 7 Experimental unsubtracted momentum-space correlation maps between the mean kinetic energy of two O^+ fragment and asymmetric parameter α as a function of delay from -45 to 405 fs, binned in time steps of 10 fs.

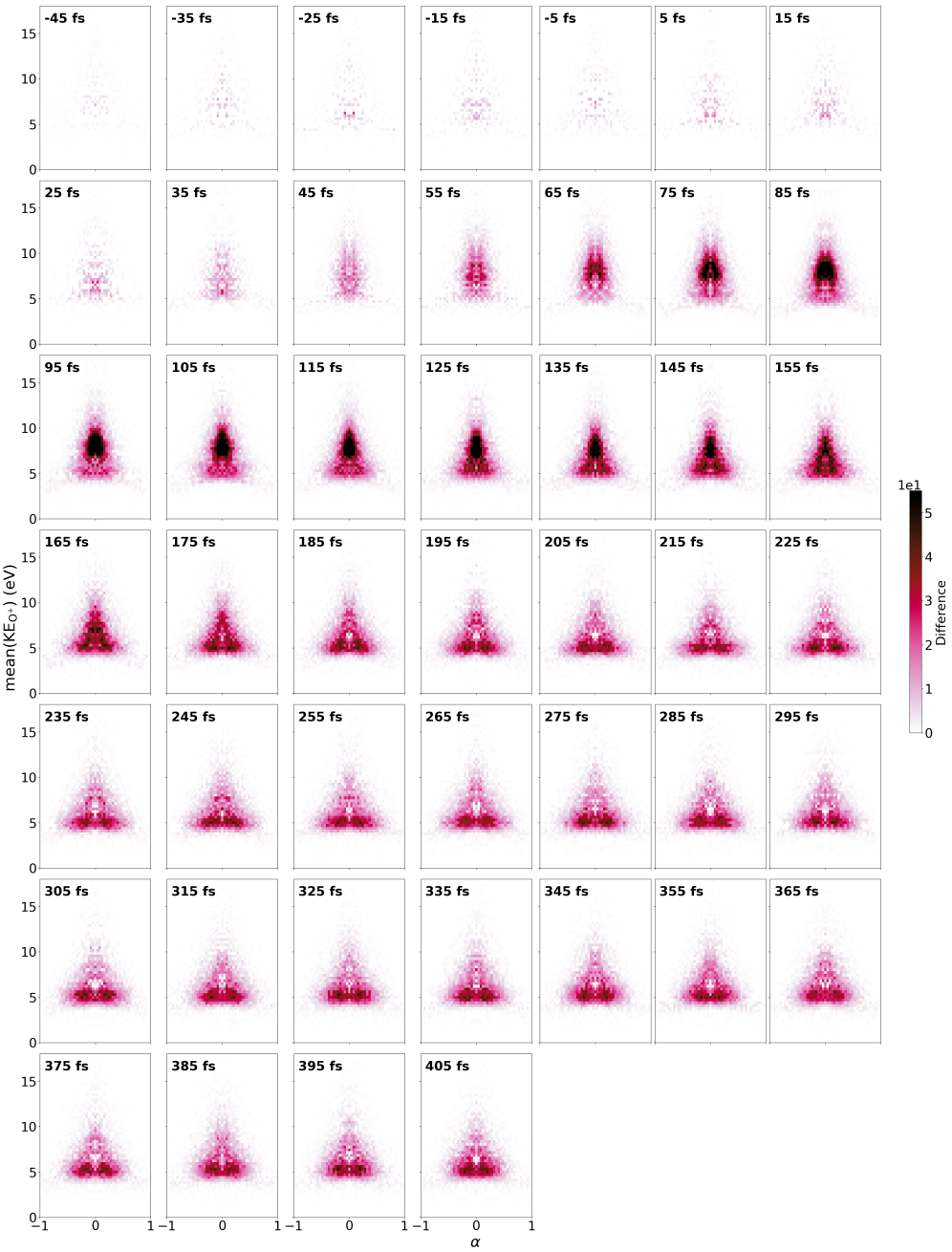

Fig. 8 Experimental subtracted momentum-space correlation maps between the mean kinetic energy of two O^+ fragment and asymmetric parameter α as a function of delay from -45 to 405 fs, binned in time steps of 10 fs. All panels show delay-dependent maps after subtraction of the mean signal recorded at negative pump-probe delay ($t < -50$ fs) to highlight pump-induced changes.

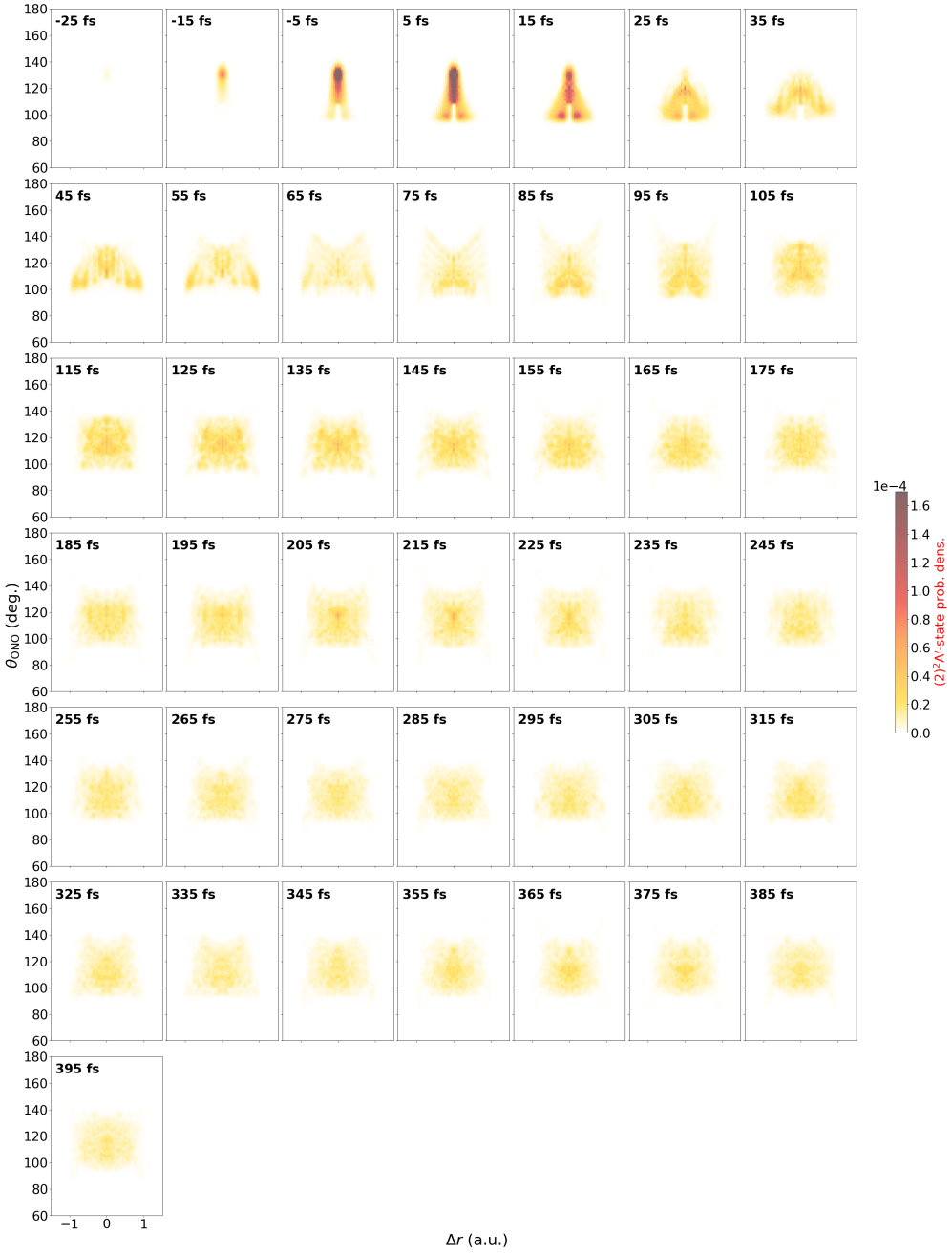

Fig. 9 Excited $(2)^2\mathrm{A}'$-state nuclear probability densities projected onto two-dimensional correlation map between the O–N–O bond angle θ_{ONO} and the asymmetric-stretch coordinate Δr. The maps are plotted as a function of delay from -25 to 395 fs, binned in time steps of 10 fs.

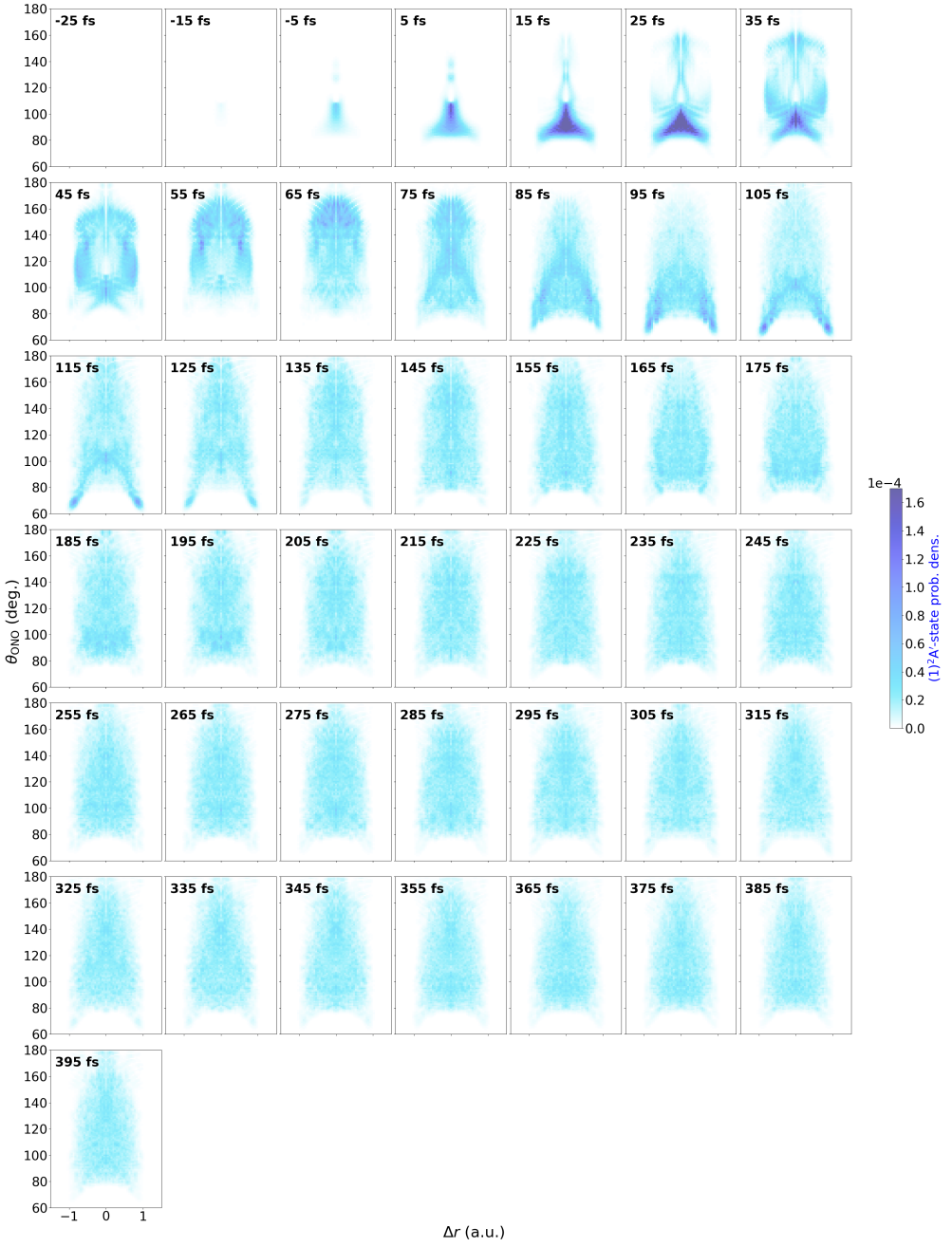

Fig. 10 Ground $(1)^2\mathrm{A}'$-state nuclear probability densities projected onto two-dimensional correlation map between the O–N–O bond angle θ_{ONO} and the asymmetric-stretch coordinate Δr. The maps are plotted as a function of delay from -25 to 395 fs, binned in time steps of 10 fs.

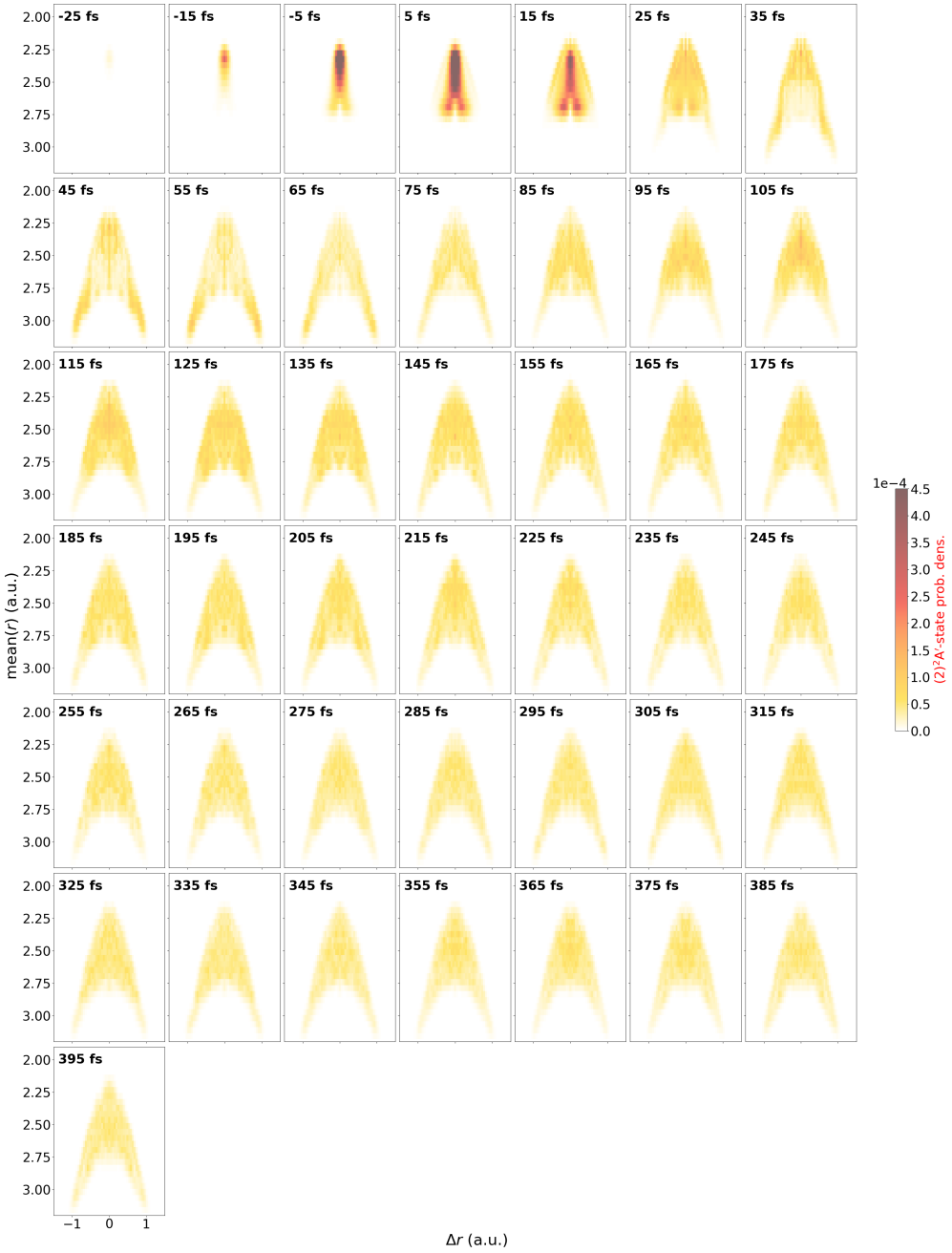

Fig. 11 Excited $(2)^2\mathrm{A}'$-state nuclear probability densities projected onto two-dimensional correlation map between the mean N–O bond length $\mathrm{Mean}(r)$ **and the asymmetric-stretch coordinate** Δr**.** The maps are plotted as a function of delay from -25 to 395 fs, binned in time steps of 10 fs.

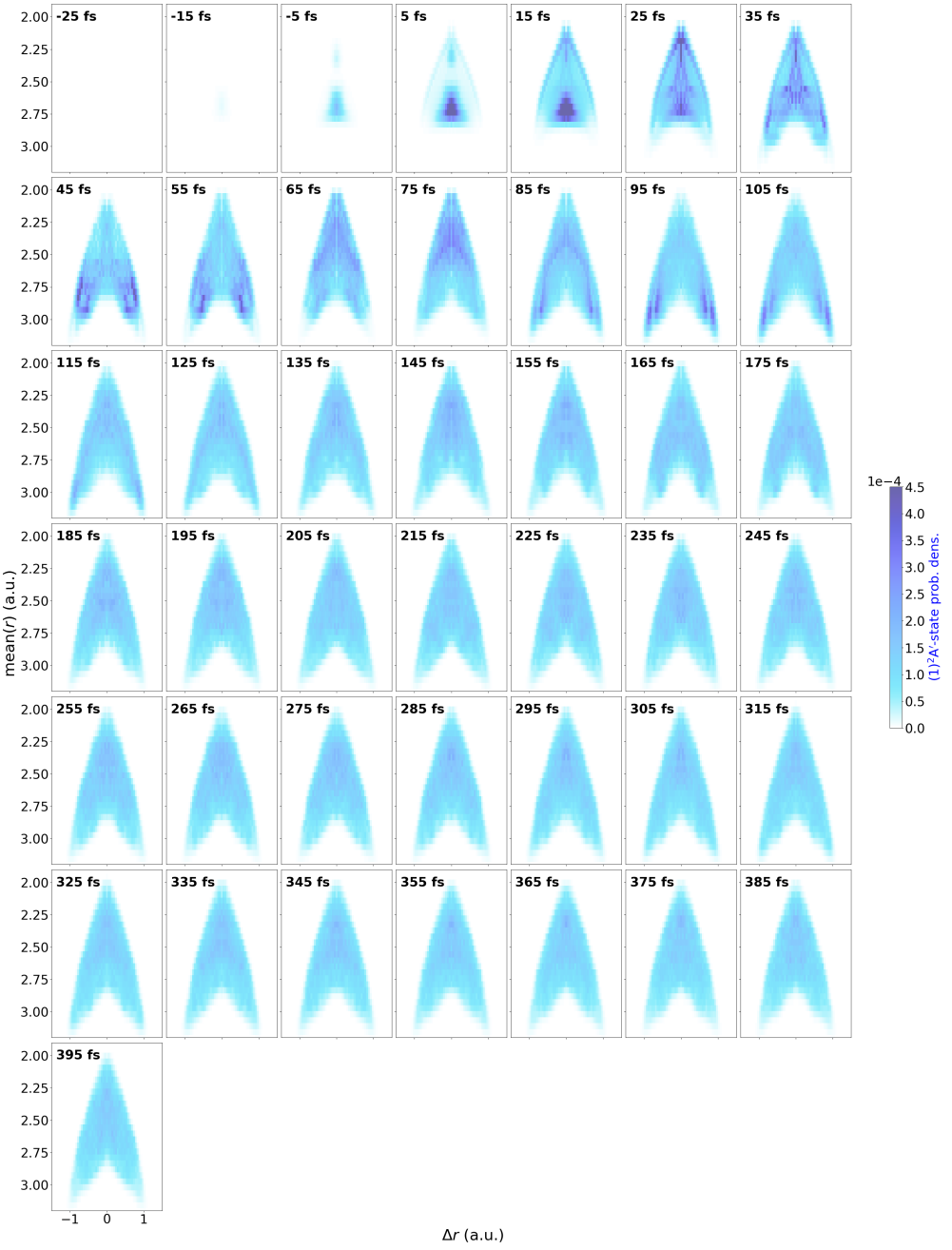

Fig. 12 Ground $(1)^2\mathrm{A}'$-state nuclear probability densities projected onto two-dimensional correlation map between the mean N–O bond length $\mathrm{Mean}(r)$ **and the asymmetric-stretch coordinate** Δr**.** The maps are plotted as a function of delay from -25 to 395 fs, binned in time steps of 10 fs.

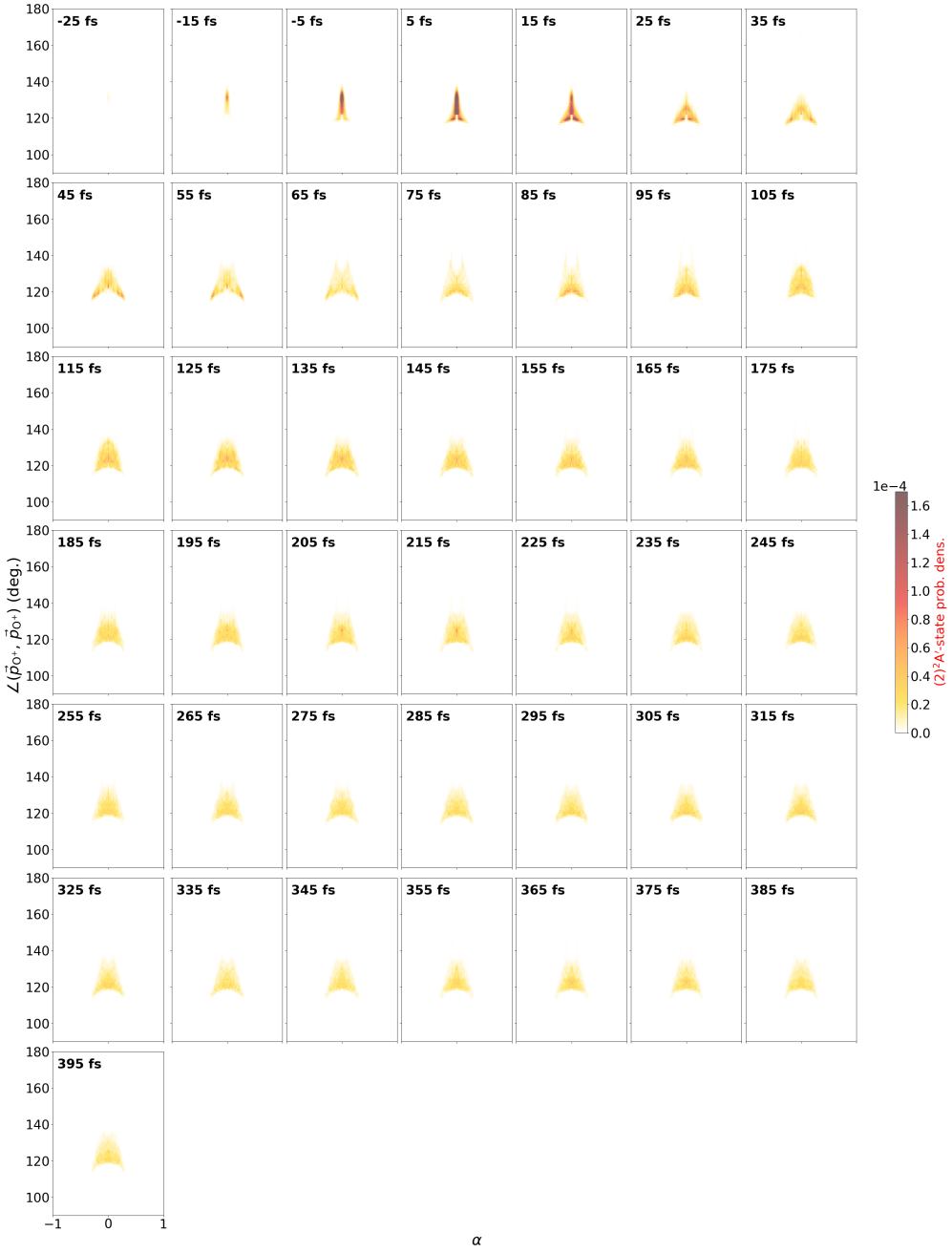

Fig. 13 Excited $(2)^2\mathrm{A}'$-state nuclear probability densities projected onto two-dimensional correlation map between the momentum-frame angle $\angle(\vec{p}_{\mathrm{O}+}, \vec{p}_{\mathrm{O}+})$ and asymmetric parameter α. The maps are plotted as a function of delay from -25 to 395 fs, binned in time steps of 10 fs.

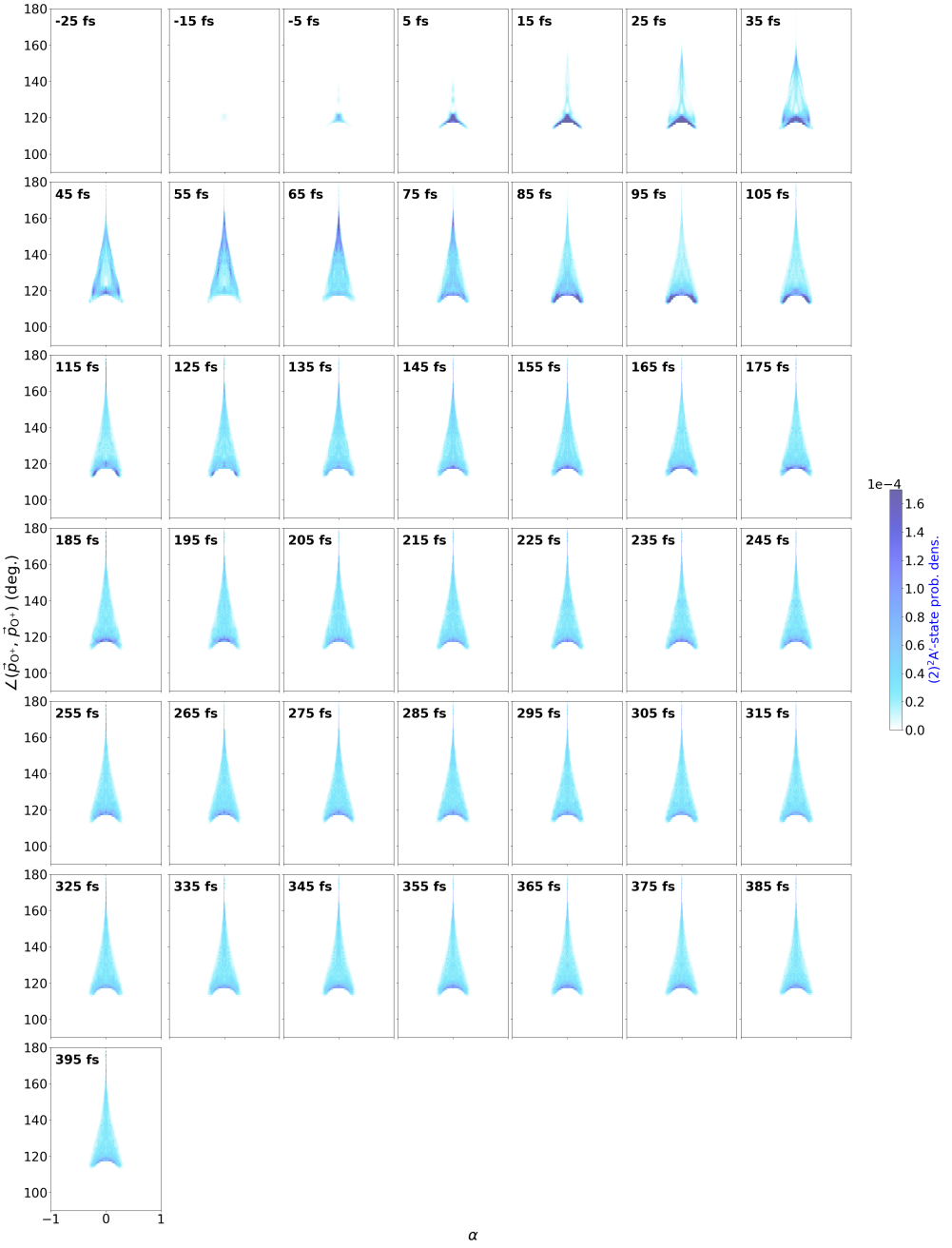

Fig. 14 Ground $(1)^2\mathrm{A}'$**-state nuclear probability densities projected onto two-dimensional correlation map between the momentum-frame angle** $\angle(\vec{p}_{\mathrm{O}^+}, \vec{p}_{\mathrm{O}^+})$ **and asymmetric parameter** α**.** The maps are plotted as a function of delay from -25 to 395 fs, binned in time steps of 10 fs.

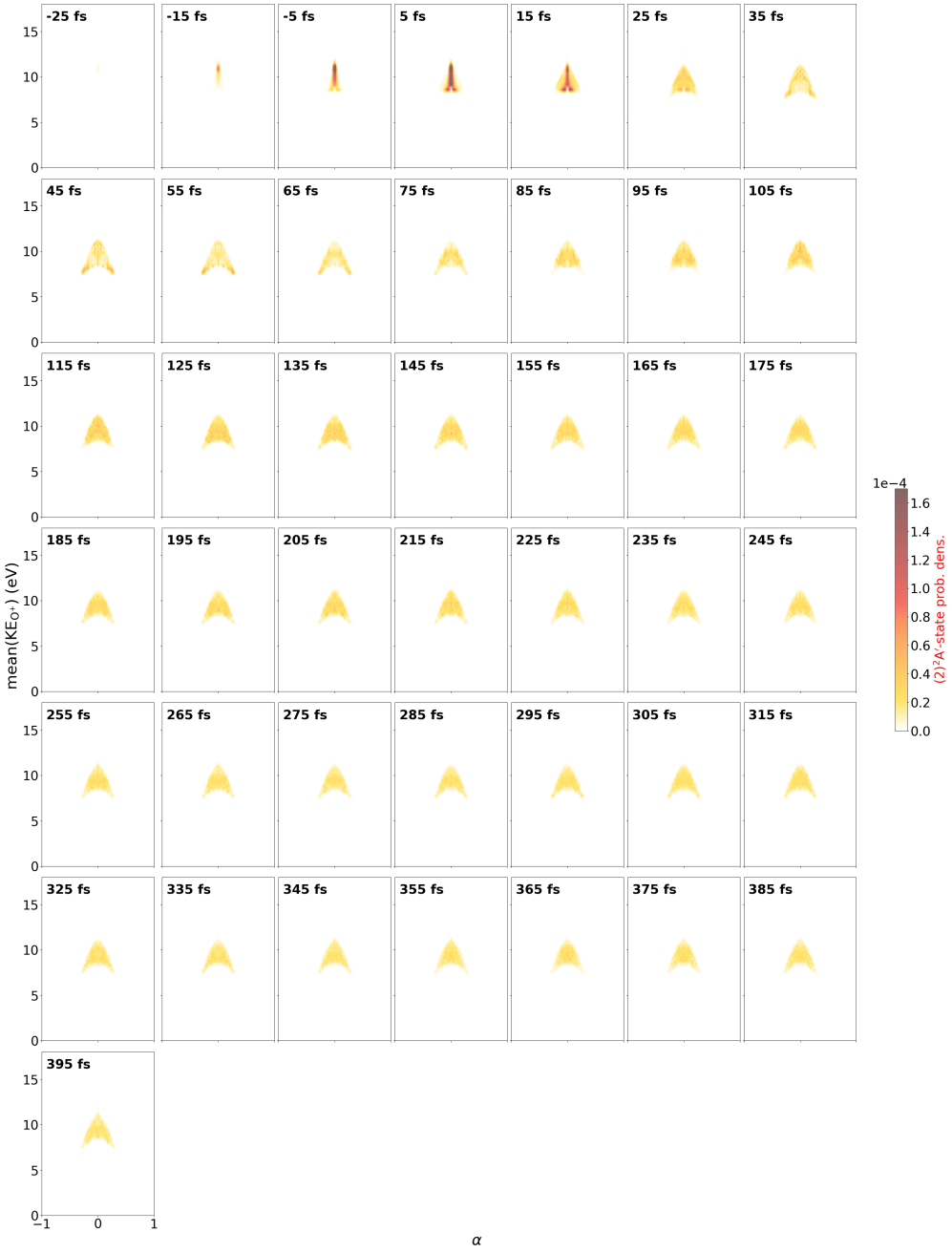

Fig. 15 Excited $(2)^2A'$-state nuclear probability densities projected onto two-dimensional correlation map between the mean kinetic energy of two O^+ fragment and asymmetric parameter α. The maps are plotted as a function of delay from -25 to 395 fs, binned in time steps of 10 fs.

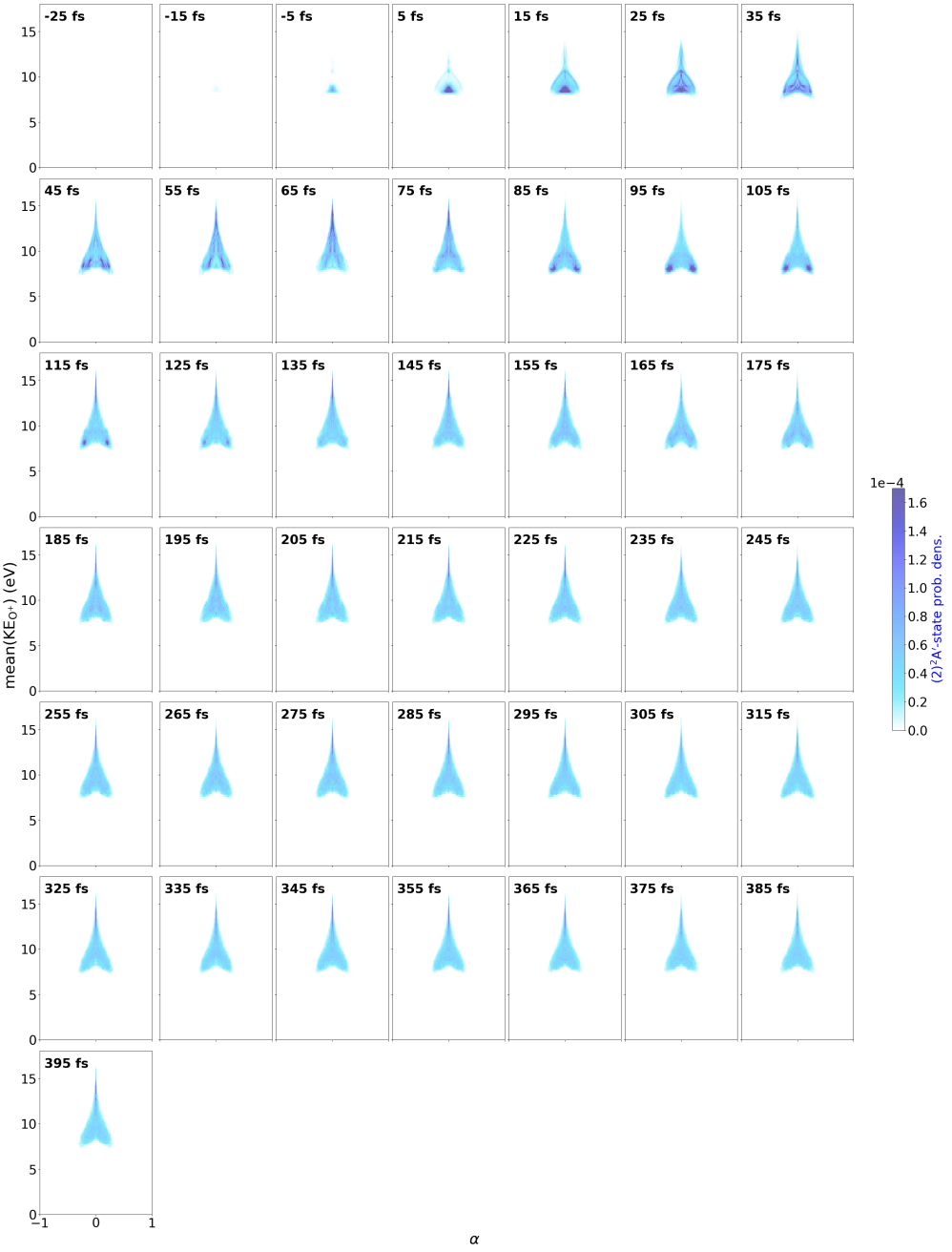

Fig. 16 Ground $(1)^2\mathrm{A}'$**-state nuclear probability densities projected onto two-dimensional correlation map between the mean kinetic energy of two** O^+ **fragment and asymmetric parameter** α**.** The maps are plotted as a function of delay from -25 to 395 fs, binned in time steps of 10 fs.

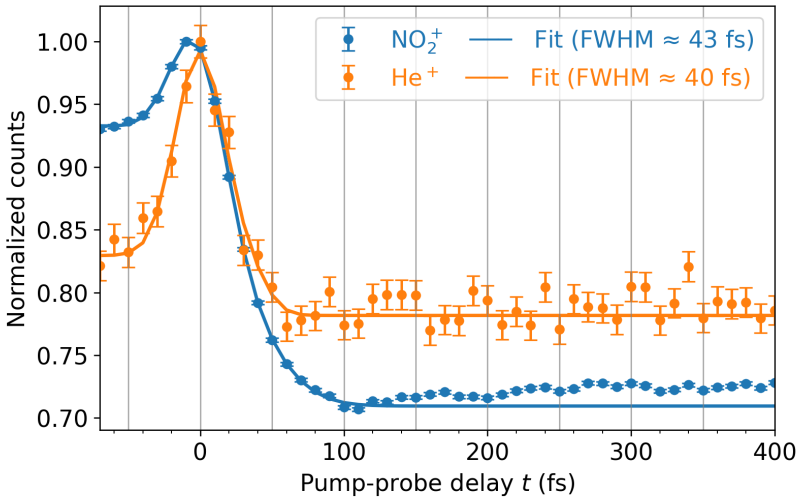

Fig. 17 Experimental 'time zero' and pump-probe cross-correlation. Yield of NO_2^+ (blue) and He^+ (orange) ions as a function of pump-probe delay t along with least-squares fits (solid lines) to determine 'time zero' and characterize the pump-probe cross-correlation width. The delay-dependent yields are fitted using a composite function defined as $f(t) = A\exp\left(-(t-t_0)^2/(2\sigma^2)\right) + (B/2)\left[1+\mathrm{erf}\left((t-\mu)/(\sqrt{2}\,\mathrm{FWHM})\right)\right] + C$, where the Gaussian term (parameters A, t_0, σ) accounts for the transient peak, and the error-function term (parameters B, μ, FWHM) describes the step-like decrease associated with ionization onset. C represents a constant offset. Here, t_0 denotes the temporal offset from zero delay, while the fitted FWHM provides an estimate of the pump–probe cross-correlation width between the UV pump and NIR probe pulses. In the case of single-photon ionization following single-photon excitation, this cross-correlation width can be used to estimate the pump pulse duration, given the known duration of the 80 nm probe pulse (28 fs). This estimate relies on the relation $\mathrm{FWHM}^2 = \tau_{\mathrm{pump}}^2 + \tau_{\mathrm{probe}}^2$, yielding an approximate pump pulse duration of ∼30 fs.

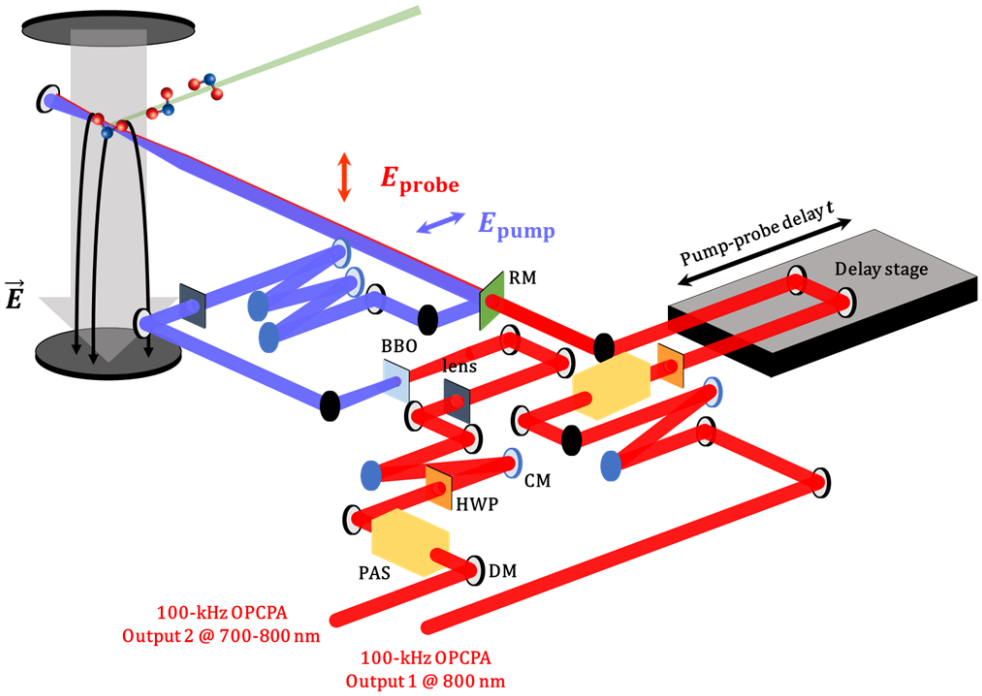

Fig. 18 Sketch of the experimental setup including the beam path of the 800-nm (red) and 400-nm (purple) laser pulses, the molecular beam (green), and the ion momentum imaging spectrometer (black). DM: dielectric mirror, PAS: power attenuator set consisting of a zero-order half-wave plate and fused-silica thin-film polarizers, HWP: half-wave plate, CM: chirped mirror, RM: recombine mirror.

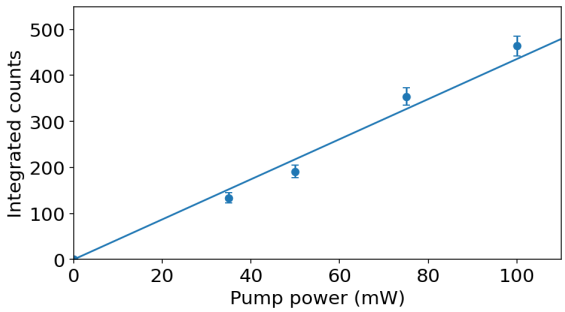

Fig. 19 Linearity of the excitation process. Integrated counts in the momentum-frame angle window of 140°–180° as a function of the power of the 400-nm pump pulses, along with a linear fit to the data points. According to **Fig. 2**, the signal observed within this angular range stems exclusively from excited molecules.

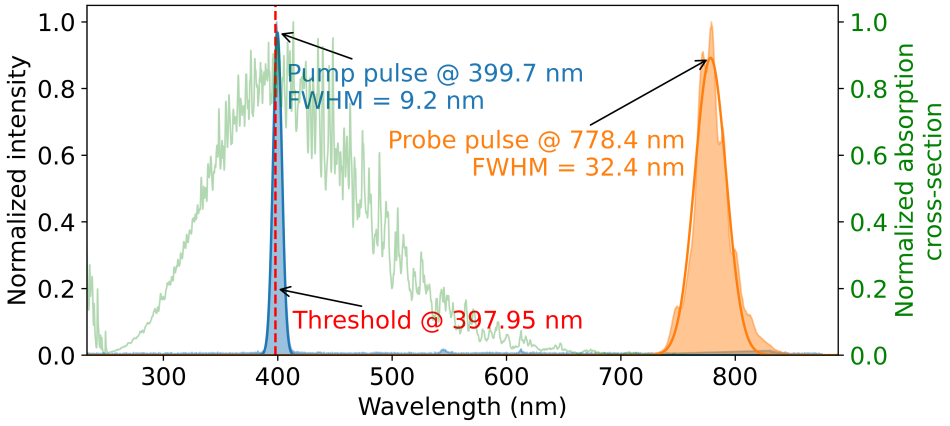

Fig. 20 NO_2 **absorption spectrum and characterization of the pump and probe pulses.** Measured spectrum of pump and probe pulses (left scale) overlaid on the NO_2 UV/VIS absorption spectrum (right scale) adapted from Ref. [1] with a red line marking the dissociation threshold.